

A&A manuscript no.
(will be inserted by hand later)

Your thesaurus codes are:
3 (02.01.2; 11.01.2; 11.14.1; 11.17.3; 12.07.1;)

ASTRONOMY
AND
ASTROPHYSICS

Microlens diagnostics of accretion disks in active galactic nuclei

A. Yonehara^{1,2}, S. Mineshige¹, J. Fukue³, M. Umemura⁴, and E.L. Turner⁵

¹ Department of Astronomy, Kyoto University, Sakyo-ku, Kyoto 606-8502, Japan

² Research Fellow of the Japan Society for the Promotion of Science

³ Astronomical Institute, Osaka Kyoiku University, Asahigaoka, Kashiwara, Osaka 582-0026, Japan

⁴ Center for Computational Physics, Tsukuba University, Tsukuba, Ibaraki 305-0006, Japan

⁵ Princeton University Observatory, Peyton Hall, Princeton, NJ 08544, USA

Received / Accepted

Abstract. The optical-ultraviolet continuum from active galactic nuclei (AGN) seems to originate from optically thick and/or thin disks, and occasionally from associated circumnuclear starburst regions. These different possible origins can, in principle, be discriminated by observations of gravitational microlensing events. We performed numerical simulations of microlensing of an AGN disk by a single lensing star passing in front of the AGN. Calculated spectral variations and light curves show distinct behavior, depending on the nature of the emitting region; time variation of a few months with strong wavelength dependence is expected in the case of an optically thick disk (*standard disk*), while an optically thin disk (*advection-dominated disk*) will produce shorter, nearly wavelength-independent variation. In the case of an associated circumnuclear starburst region much slower variations (over a year) will be superposed on the shorter variations caused by microlensing of the disk.

Key words: accretion, accretion disks — active galactic nuclei — microlensing

1. Introduction

There has been long discussion regarding the central structure of active galactic nuclei (AGN). Generally, it is believed that there is a supermassive black hole and a surrounding accretion disk. However, it is quite difficult to obtain direct information about the center of AGN, the accretion disk, because the disk size is far too small to resolve. As for cosmological objects, e.g., quasars, the (angular diameter) distance is of the order of $\sim 1\text{Gpc} \sim 3 \times 10^{27}\text{cm}$. If a black hole placed at the center has a mass of $\sim 10^8 M_\odot$, the disk size (say $\sim 1000 r_g$, where r_g is Schwarzschild radius) will be $\sim 3 \times 10^{16}\text{cm}$. Hence, apparent disk size (θ_{disk}) is only $\sim 10^{-11}\text{radian} \sim 1\mu\text{as}$.

Send offprint requests to: A. Yonehara

Correspondence to: yonehara@kusastro.kyoto-u.ac.jp

What is usually done is to observe the spectra, which are the sum of local spectra over the entire disk, and to make a fitting to the observed spectra by theoretically integrated spectra. However, there remain ambiguities as to the spatial emissivity distribution. The standard picture is that the so-called UV bump is attributed to blackbody radiation from the standard-type, optically-thick disks (i.e., Shakura & Sunyaev 1973). Such a fundamental belief may be reconsidered by the recent HST observations that show no big blue bumps (e.g., Zheng et al. 1997).

Instead, microlensing can be used as a ‘gravitational telescope’ to resolve the disk structure (see Blandford & Hogg 1995; originally proposed by Chang & Refsdal 1984), since a typical Einstein-ring radius of a stellar mass lens is very small; e.g., $\theta_E \sim 10^{-11}\text{radian}$ for cosmological distant sources. With such a gravitational telescope we may be able to obtain information about the disk emergent spectra as a function of the distance from the central black hole.

When a point source object is lensed, its luminosity is amplified without any color change. This feature is called ‘achromaticity’ and is discussed in many literature, initiated by Paczyński (1986; for a review see Narayan & Bartelmann 1996). But, in some actual situations, we cannot treat a source as a point and the effect of a finite source size should be taken into account. Grieger, Kayser & Refsdal (1988) examined such finite size effects. They simulated microlensing light curves for two different source profiles: stellar like and accretion disk like. The light curves show distinct shapes from those of point source calculations. However, they only considered monochromatic intensity variation. Later, Wambsganss & Paczyński (1991) pointed out that if the finite size source has inhomogeneous structure so that each part produces a different spectrum, lensing light curves have wavelength dependence; i.e., chromatic features in microlensing events should appear. This chromatic effect has been investigated by several authors who calculated microlensing light curves of AGN accretion disk based on simple disk models

(e.g., Rauch & Blandford 1991; Jaroszyński, Wambsganss & Paczyński 1992).

The purpose of this paper is to obtain some criteria for distinguishing disk physics based on more realistic disk models, we adopt the optically-thick, standard-type disk and the most successful, optically thin disk model, the advection-dominated accretion flow (ADAF; Narayan & Yi 1995; Abramowicz et al. 1995). So far nobody (except Yonehara et al. 1998) has yet calculated X-ray or radio emission in the microlens events, due probably to the lack of reliable disk models. However, such calculations are of great importance since X-ray and radio emission seems to originate from the vicinity of a putative black hole. In section 2 we describe our methods of simulation. In section 3 our results are displayed. Section 4 is devoted to discussion.

2. Method of the simulation

2.1. Accretion disk models

First, we describe the adopted accretion disk models. We consider two representative types of disks:

1. Optically thick disk:

The first case we consider is the geometrically-thin and optically-thick standard disk (Shakura & Sunyaev 1973). Since we are concerned with disk structure on scales ranging from a few tens to a few thousands of r_g , we ignore relativistic effects, such as the gravitational redshift by the black hole, for simplicity. The temperature distribution of the optically thick standard disk is then given by (Shakura & Sunyaev 1973)

$$T(r) = 2.2 \times 10^5 \left(\frac{\dot{M}}{10^{26} \text{ g s}^{-1}} \right)^{1/4} \left(\frac{M}{10^8 M_\odot} \right)^{1/4} \times \left(\frac{r}{10^{14} \text{ cm}} \right)^{-3/4} \left[1 - \left(\frac{r_{\text{in}}}{r} \right)^{1/2} \right]^{1/4} \text{ K}, \quad (1)$$

where \dot{M} is the mass accretion rate and M is the black hole mass. The inner edge of the disk, r_{in} , is set to be $r_{\text{in}} = 3r_g$, the radius of the marginally stable last circular orbit around a non-rotating black hole.

Since the disk is optically thick, we can assume black-body radiation. Inserting the temperature profile $T(r)$ into

$$\Delta L(\nu, r) = 2 \cdot 4\pi B_\nu [T(r)] \Delta S \cos \alpha, \quad (2)$$

we can calculate the luminosity of a part of the disk with the surface element, $\Delta S = \Delta r \cdot r \Delta \phi$, at a radius r and a frequency ν , where B_ν is a Planck function (e.g., see eq.(1.51) of Rybicki & Lightman 1979), and α is the inclination angle of the disk. For simplicity, here, we assume the disk is face-on ($\alpha = 0$). It might be noted that the radiation spectra do not depend on the viscosity in this standard-type disks, since the total emissivity and the effective temperature are solely determined by the energy

balance between the radiative cooling and viscous heating (which originates from release of gravitational energy).

2. Optically thin disk

The second model is the optically thin version of the advection dominated accretion flow (ADAF). We used the spectrum calculated by Manmoto, Mineshige, & Kusunose (1997) and derive luminosity $\Delta L(\nu, r)$ in the same way as we did for an optically thick disk:

$$\Delta L(\nu, r) = 2 \cdot \epsilon_\nu(r) \Delta S, \quad (3)$$

where ϵ_ν is surface emissivity which include the effect of inclination angle (details are given in Manmoto et al. 1997). In this paper, we also set $\alpha = 0$ (face-on) same as the case of optically thick disk. Here, included are synchrotron, bremsstrahlung, and inverse Compton scattering of soft photons created by the former two processes (see Narayan & Yi 1995 for more details). Optical flux is mainly due to Comptonization of synchrotron photons.

In this sort of disks (or flows), radiative cooling is inefficient because of very low density. As a result, accreting matter falls into a central object, hardly losing its internal energy (which is converted from its gravitational energy through the action of viscosity) in a form of radiation. Hence, although the total disk luminosity is less than that of the standard one for the same mass-flow rate, the disk can be significantly hotter, with electron temperatures being of the order of 10^9 K or more, thus producing high energy (X- γ ray) photons. Photon energy is thus widely spread over large frequency ranges. Since emission inside the last circular orbit (at $3r_g$) is not totally negligible in this case, we solve the flow structure until the event horizon (r_g) passing through the transonic point, and consider radiation from the entire region outside the horizon, although the contribution from the innermost part is not dominant. Unlike the optically thick case, the viscosity explicitly affects the emissivity in this case, since radiative cooling depends on density and is no longer balanced with viscous heating (and with gravitational energy release). In the present study, we assign the viscosity parameter to be $\alpha = 0.1$.

2.2. Microlensing events

Although single lens approximation is not always appropriate to the microlensing events, we, here, use this simple method because of making the situation clear (for extend source effect of microlensing by single lens object, e.g., Bontz 1979).

Generally, the microlensed images are split into two (or more) images. When the separation between these images is too small to resolve, however, the total magnitudes of all the split images vary due to this microlensing caused by the relative motion of lens and source.

The properties of microlensing have been extensively examined for simple cases where both the lens and source are regarded as being points (e.g., Paczyński 1986). In our

simulation, we include an effect of occultation by a lens object which is recently included the simulation of microlens light curves by Bromley (1996) for reality. In other words, we, here, consider that the radius of the lens object (R_{lens}) is same as the sun, i.e., $R_{\text{lens}} = R_{\odot} = 6.96 \times 10^{10}$ cm, and calculate image positions of the all cell. If the image position of a cell from the lens object is smaller than the radius of lens object, we exclude a contribution from that image. Therefore, the total amplification (or magnification) factor A for microlensing is exactly expressed as

$$A(u) = \begin{cases} 0 & (\theta_{\text{image},+} < \frac{R_{\text{lens}}}{D_{\text{ol}}}) \\ \frac{u^2+2}{2u(u^2+4)^{1/2}} + \frac{1}{2} & (\theta_{\text{image},-} < \frac{R_{\text{lens}}}{D_{\text{ol}}} \leq \theta_{\text{image},+}) \\ \frac{u^2+2}{u(u^2+4)^{1/2}} & (\text{otherwise}), \end{cases} \quad (4)$$

where u corresponds to the angular separation between lens and source in the unit of the Einstein-ring radius and always greater than or equal to zero, i.e., $u \geq 0$, and $\theta_{\text{image},\pm}$ shows that the image positions of two microlensed images from a lens object in the unit of radian, i.e.,

$$\theta_{\text{image},\pm} = \frac{1}{2}\theta_E \left[u - (u^2 + 4)^{1/2} \right] \quad (5)$$

This function as shown in eq. 4 is a monotonically increasing function of u ; $A(u) \simeq 1.34, \sim 10, \sim 100$ for $u = 1.0, 0.1$, and 0.01 .

Here, the Einstein-ring radius is

$$\theta_E = \left(\frac{4GM_{\text{lens}}}{c^2} \frac{D_{\text{ls}}}{D_{\text{os}}D_{\text{ol}}} \right)^{1/2} \quad (6)$$

where M_{lens} is the mass of a lensing star, c is the speed of light, G is the gravitational constant, and $D_{\text{ls}}, D_{\text{os}}$, and D_{ol} denote the angular diameter distances from lens to source, from observer to source, and from observer to lens, respectively (Paczynski 1986). Adopting an appropriate cosmological model, we can calculate these angular diameter distances in terms of redshifts z_{ls} (from lens to source), z_{os} (from observer to source), and z_{ol} (from observer to lens). In the present study, we assume the Einstein-de Sitter Universe, in which we have

$$D_x = \frac{2c}{H_0} \frac{1}{1+z_x} \left[1 - \frac{1}{(1+z_x)^{1/2}} \right] \quad (7)$$

(e.g., Padmanabhan 1993), where H_0 is Hubble's constant, and the subscript 'x' stands for 'ls', 'os', or 'ol'.

Since we now consider microlensing effects on an extended source, we must integrate the magnification effects over the entire source plane. We thus, as a next step, need to calculate the angular separation u between a part of the source in question and the lens center (see figure 1), from which the amplification factor, $A(u)$, can be found. In the present study, we first divide an accretion disk plane into azimuthal (ϕ) and radial (r) elements. The azimuthal coordinate is equally divided into ~ 1000 segments (ϕ_j),

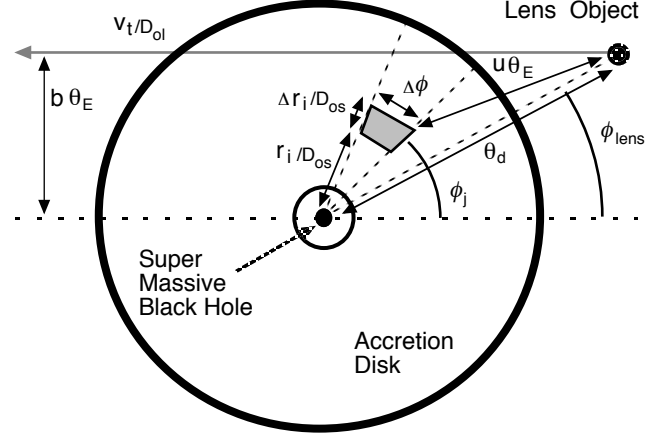


Fig. 1. Schematic view of calculation for the separation between each cell and lens.

while the logarithmically scaled radial coordinate is also equally divided into ~ 1000 segments (r_i). We then calculate the observed flux at frequency ν from a cell between r_i and r_{i+1} in the radial direction and between ϕ_j and ϕ_{j+1} in the azimuthal direction. Noting that photons emitted by the source at a frequency ν are observed at the frequency $\nu/(1+z_{\text{os}})$, we write the observed flux as

$$\Delta F_{\text{obs}}(\nu; r_i, \phi_j) \simeq A(u) \Delta F_{\text{obs},0}[\nu(1+z_{\text{os}}), r_i, \phi_j], \quad (8)$$

where $A(u)$ is the amplification factor given by equation (4). Moreover, u is explicitly given by

$$u = \left[\left(\frac{r_i}{D_{\text{os}}} \cos \phi - \theta_d \cos \phi_{\text{lens}} \right)^2 + \left(\frac{r_i}{D_{\text{os}}} \sin \phi - \theta_d \sin \phi_{\text{lens}} \cos \alpha \right)^2 \right]^{1/2} \theta_E^{-1}, \quad (9)$$

where α is the inclination angle of an accretion disk (in this paper, as indicated in §2.1, we set $\alpha = 0$), and θ_d and ϕ_{lens} represent the radial and the azimuthal positions of the lens in units of radians, respectively. Schematic view of the calculated disk is shown in figure 1. The intrinsic flux in the absence of a microlensing event, $\Delta F_{\text{obs},0}(\nu, r)$, is calculated from $\Delta L(\nu, r)$ according to

$$\Delta F_{\text{obs},0}(\nu, r) = \frac{\Delta L(\nu, r)}{4\pi D_{\text{os}}^2 (1+z_{\text{os}})^3}, \quad (10)$$

and $\Delta L(\nu, r)$ depends on the disk model (see eq. (2) and (3)). In the present study, since we neglected the relativistic effect (e.g., beaming, gravitational redshift etc.), $\Delta L(\nu; r, \phi)$ has no azimuthal dependence.

Summing up $\Delta F_{\text{obs}}(\nu; r, \phi)$ over the entire disk plane from the inner boundary (r_{in}) to the outer boundary (r_{out}), we obtain the total observed flux at frequency ν , or the spectrum of the microlensed accretion disk.

3. Results of the calculations

3.1. Model parameters

For clarity, we consider a lensed quasar, Q 2237+0305 (the Einstein cross, e.g., Huchra et al. 1985). Irwin et al. (1989) reported an increase of the apparent luminosity of image A by ~ 0.5 mag on a timescale of a few months, which was nicely reproduced by a model of microlensing (Wambsganss, Paczyński, & Schneider 1990). At present, at least five microlens events have been reported so far on the split images (Irwin et al. 1989; Corrigan et al. 1991; Houde & Racine 1994). Although the single lens treatment for Q 2237+0305 may be a poor approximation (see discussion), we just take this object as one test case and derive quite general conclusions regarding the generic observational features of microlensed accretion disks.

This object is macrolensed by a foreground galaxy, and the source is split into four (or five) images. Now, we suppose that one of the macrolensed image is further microlensed by a star in the foreground galaxy causing the macrolensing. Although the macrolensed images are actually affected by two effects, so called, ‘convergence’ and ‘shear’, we here neglect both for simplicity and thus assume that the macrolensed image is neither amplified nor distorted. The redshift parameters are

$$z_{\text{os}} = 1.675, \quad z_{\text{ol}} = 0.039 \quad (11)$$

(cf. Irwin et al. 1989), and substitute them into the relation

$$1 + z_{\text{ls}} = \frac{1 + z_{\text{os}}}{1 + z_{\text{ol}}} \quad (12)$$

which can be obtained from flux conservation of radiation (e.g., Padmanabhan 1993), we get

$$z_{\text{ls}} = 1.575. \quad (13)$$

As for Hubble’s constant, we adopt the value obtained by Kundić et al. (1997), $H_0 \sim 60 \text{ km s}^{-1} \text{ Mpc}^{-1}$. The adopted disk parameters are the outer edge of the disk, $r_{\text{out}} = 10^3 r_g$, the mass of the central black hole, $M = 10^8 M_\odot$, and the mass-flow rates, $\dot{M} = 10^{26} \text{ g s}^{-1}$ for the standard disk and $\dot{M} = 10^{22} \text{ g s}^{-1}$ for the optically thin disk. We take different mass-flow rates for two cases because of calculation convenience. This is not, fortunately, a serious problem, since it has been demonstrated that the spectral shape of the ADAF is not very sensitive to \dot{M} , although the overall flux level does change. We will not discuss the absolute flux in the following discussion, and focus on the relative spectral shape and relative flux variation. For other basic parameters characterizing the disks, see §2.1.

For simplicity, we assume that the accretion disk is face-on; i.e. $i = 0$, to the observer. Actually, based upon a grand unified paradigm of AGNs, quasars are not far from face-on views. We also assume the mass of a lensing object

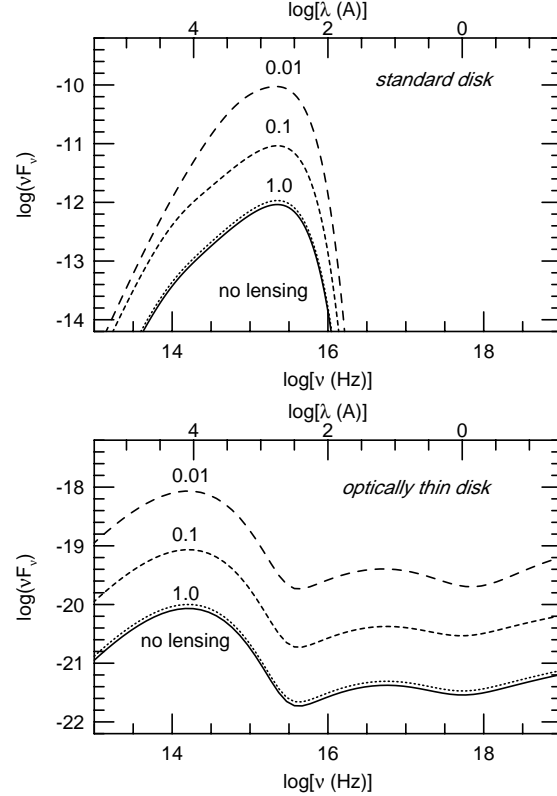


Fig. 2. Microlensed spectrum of a standard accretion disk (upper) and an optically thin accretion flow (lower). In each panel, the microlensed spectra are plotted for angular separations between the disk center and the lensing star to be $u = 1.0$ (dotted line), 0.1 (dashed line), and 0.01 (long dashed line), together with the one in the absence of microlensing (solid line). The lensing mass is $M_{\text{lens}} = 1.0 M_\odot$.

to be $M_{\text{lens}} = 1.0 M_\odot$ or $0.1 M_\odot$. The remaining variable is the angular separation (u) between the lens and a part of the source in question.

Adopting these parameters, apparent angular accretion disk size (θ_{disk}) and Einstein ring radius (θ_E) is $\theta_{\text{disk}} \sim 6.8 \times 10^{-12} \text{ rad}$ and $\theta_E \sim 3.3 \times 10^{-11} \text{ rad}$. These values are comparable and we, here, can use microlensing event as effective ‘gravitational telescope’ (Blandford & Hogg 1995).

3.2. Spectral variation

First, we calculated the microlensed spectra of each of two types of accretion disks for the angular separation between the lens and the source of $u = 1.0$, 0.1 , and 0.01 , respectively. The results are shown in figure 2 for the standard disk (in the upper panel) and for the optically thin disk (in the lower panel), respectively. For the former disk not only the disk brightening, but also substantial spectral de-

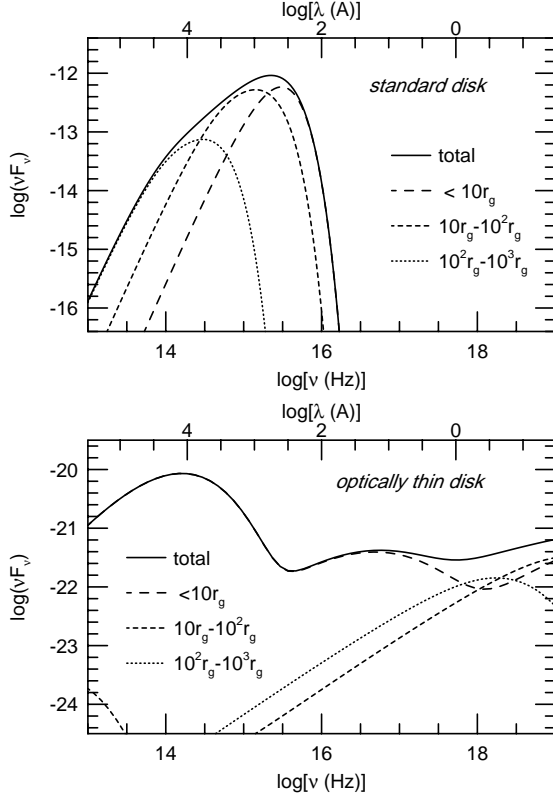


Fig. 3. Contribution to the total integrated spectra from different parts of disks for the cases of a standard (upper) and optically thin (lower) disk, respectively. Each figure displays the contributions from the inner region of $r \leq 10r_g$ (long dashed line), the intermediate region of $10r_g \sim 100r_g$ (dashed line), and the outer region of $10^2r_g \sim 10^3r_g$ (dotted line).

formation is produced by microlensing, when the angular separation is small (Rauch & Blandford 1991; Jaroszyński, Wambsganss & Paczyński 1992). The smaller the angular separation is, the larger becomes the modification of the observed spectrum. In other words, the amplification factor depends on the frequency (wavelength) of the emitted photons. This gives rise to frequency-dependent, microlensing light curves (see §3.3). As for the optically thin disk, in contrast, there will not be large spectral modification by microlensing, but the flux is amplified over wide frequency ranges.

To understand such spectral properties, we divide the disk plane into three parts; $r \leq 10r_g$, $10r_g < r < 100r_g$, and $10^2r_g < r < 10^3r_g$, and plot the spectrum from each part of the disk, together with the integrated spectra, in figure 3.

In the case of the optically thick accretion disk, photons emitted from different radii have different dominant frequencies because the local temperature of the disk has a strong radial dependence, $T \propto r^{-3/4}$ (Eq. [1]). Note

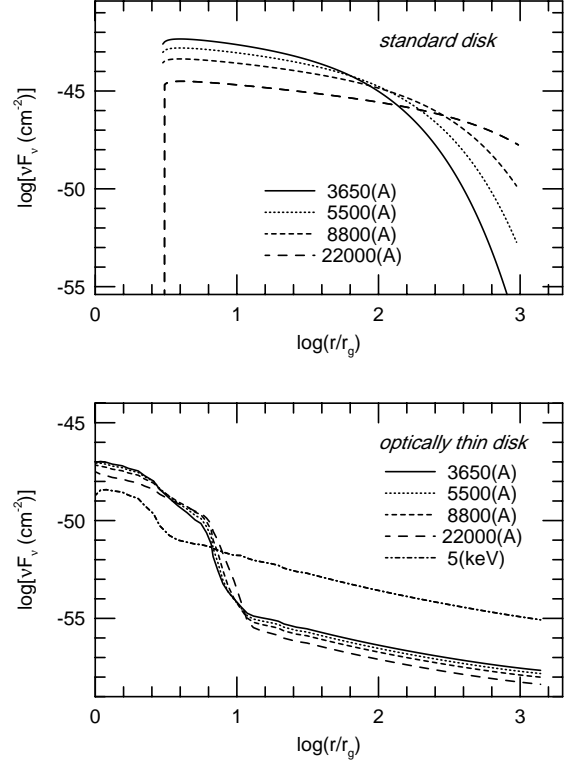


Fig. 4. The radial distribution of the emergent flux with several wavelengths for the case of a standard-type disk (upper) and an optically thin disk (lower), respectively. The adopted bands are U-band (3650 Å, by the solid line), V-band (5500 Å, by the dotted line), I-band (8800 Å, by dashed line), K-band (22000 Å, by long dashed line), and X-ray (5 keV, by the dot-dashed line).

that without lensing the total spectrum has a peak at $\nu \sim 10^{15.3}$ Hz, but its low-frequency part has a smaller slope ($\nu F_\nu \propto \nu^{4/3}$) than that of blackbody radiation ($\nu F_\nu \propto \nu^3$), thus a shoulder like feature extending to $\nu \sim 10^{14}$ Hz ($\sim 30000\text{Å}$) being formed. This is because the outer cooler portions also contribute to the spectrum. For $u = 0.01$, therefore, the emission only from the inner, hottest part is strongly magnified, much strengthened a peak at $\nu \sim 10^{15.3}$ Hz ($\sim 1500\text{Å}$) and a shoulder like feature at $\nu \sim 10^{14}$ Hz ($\sim 30000\text{Å}$) appears to be weakened. Consequently, microlensed spectrum became a form with one sharp peak.

To help understanding such situation, we also plot the radial distribution of emitted photons with several wavelengths in figure 4. The upper panel of figure 4 shows rather gradual change of each flux over a wide spatial range. This reflects the fact that viscous heating and radiative cooling are balanced in the standard disk. Since the potential energy only gradually changes with the radius, so is the viscous heating rate and is the radiative

cooling rate. Moreover, the lower a photon frequency is (or the longer the wavelength is), the wider becomes the parts of the disk which generate photons.

In the optically-thin accretion disk, on the other hand, the optical-UV flux is totally dominated by that from the inner region ($r \leq 10r_g$). The lower panel of figure 4 clearly shows that almost 100% of optical flux originates from the region inside $10r_g$, and that the contribution from the outer parts is smaller by several orders. This is possible in ADAF, since radiative cooling is no longer directly related to the shape of the gravitational potential well (which has a rather smooth profile). The reason why optical flux is produced in a rather restricted region inside $10r_g$ is due to enhanced synchrotron emission in the vicinity of the black hole, where density and pressure (and thus magnetic pressure) are likely to be at maximum within the flow. Nearly irrespective of the u value, as a consequence, it is always the innermost region (within $10r_g$) that dominates the entire disk spectrum. The amplification of the total emission just reflects that of the emission from the innermost parts. Therefore, the overall flux will be amplified by lensing without large spectral changes.

Figure 4 also shows that X-rays are produced over a wider range; the contribution from the outer part at $100 - 1000r_g$ is not negligible at frequency of $f \sim 10^{18}$ (a few keV). This is because of a bremsstrahlung emission from high-temperature electrons (with $T_e \sim 10^9 K$ being maintained at $r \lesssim 100r_g$, see Manmoto et al. 1997). We can thus predict that small frequency dependence will be seen in X-ray ranges in this model.

Such distinct spectral behaviors give rise to different light curves of the two disk models (see below).

3.3. Light curves

Using the results of the previous subsection, we now calculate the light curve during the microlensing events (see fig. 1). We continuously change the angular separation between the lens and the center of the accretion disk (θ_d) according to

$$\theta_d = \theta_d(t) = \theta_E \left[b^2 + \left(\frac{v_t t}{D_{ol} \theta_E} \right)^2 \right]^{1/2}, \quad (14)$$

and calculate the flux at each frequency, where b is the impact parameter (in the unit of θ_E), v_t is the transverse velocity of the lens and t is the time. Note that v_t also includes the transverse velocity due to the peculiar motion of the foreground galaxy relative to the source and the observer. We calculated three cases (see fig. 5).

Figure 6 shows the microlensing light curves of optically thick (upper panel) and thin (lower panel) disks for the case with $(b, M_{\text{lens}}) = (0.01, 1.0M_\odot)$ (Case 1). The light curve of the optically thin disk is still achromatic because of its flat temperature distribution, whereas the

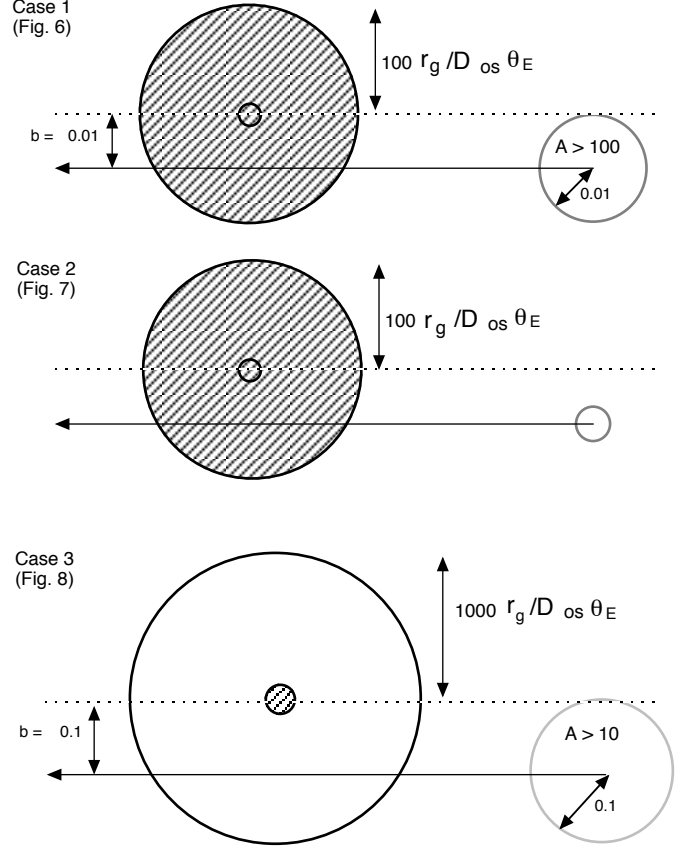


Fig. 5. Schematic view of the microlensing events which we have calculated. These figures show the relative sizes of the accretion disk, impact parameter, tracks which lens object passes, and the Einstein-ring radius. In each panel, shaded regions correspond to the disk with a radius of $100r_g$. Top panel (Case 1) shows microlensing event of $(b, M_{\text{lens}}) = (0.01, 1.0M_\odot)$. Left, thick outer and inner circles corresponds to the radius of $100r_g$ and $10r_g$, respectively. A right circle corresponds to $\sim 0.01\theta_E$. Inside this circle, the amplification factor caused by microlensing is more than 100. Middle panel (Case 2) shows microlensing event of $(b, M_{\text{lens}}) = [0.01(M_\odot/M_{\text{lens}})^{1/2}, 0.1M_\odot]$. The types of left circles are the same as those in the top panel. Bottom panel (Case 3) shows microlensing event of $(b, M_{\text{lens}}) = (0.1, 1.0M_\odot)$. Left, thick outer and inner circles corresponds to $1000r_g$ and $100r_g$ of accretion disk. A right circle corresponds to $\sim 0.1\theta_E$, amplification factor caused by microlensing is more than ~ 10 .

light curve of the optically thick one shows strong frequency dependence.

Figure 4 is again useful to understand this chromaticity and achromaticity. Since flux distribution is similar among different optical fluxes in the case of optically thin disks, each optical flux is amplified in a similar way and thus the color does not change; i.e. achromatic feature appears. X-ray emitting region is wider than that of optical flux,

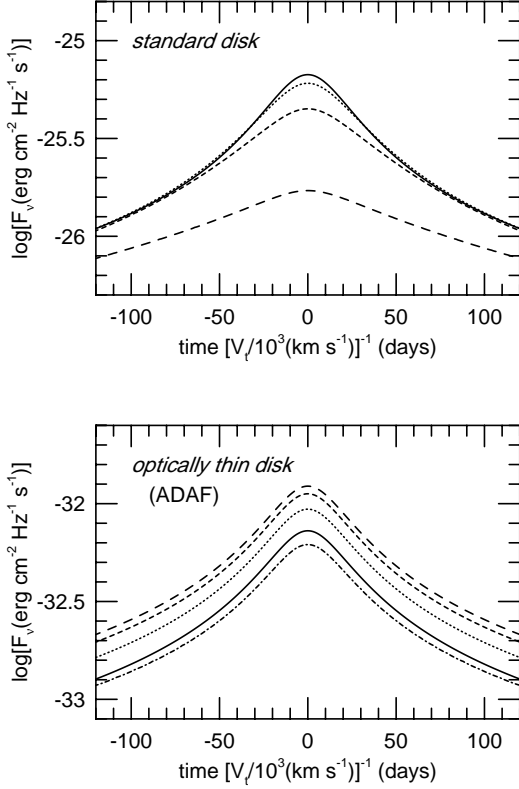


Fig. 6. The microlensed light curves of the standard disk (upper) and for the optically thin flow (lower). The parameters are $(b, M_{\text{lens}}) = (0.01, 1.0 M_{\odot})$ (Case 1). The different type of lines correspond to the same as in figure 4.

small chromaticity may appear when we compare optical and X-ray light variations.

In an optically thick disk, conversely, low-energy photons are created in a wider spatial range, compared with high-energy photons. If the microlensing event occurs, therefore, low-energy emission will be the first to be amplified, followed by the significant amplification of high-energy emission. Note that each optical flux has the same level at the beginning (at -120 day) in the upper panel of figure 6, whereas a higher-energy optical flux is greater than that of a lower-energy flux in the intrinsic spectra in the absence of lensing (see figure 3). This indicates that the amplification of a lower-energy flux has already been appreciable at $t = -120$ day. This results in the color change; i.e. chromatic feature is produced.

3.4. Parameter dependence

Figure 7 shows the light curves for the case with a smaller lensing mass by one order and the same physical impact parameter ($b\theta_E$) (Case 2). Namely, $(b, M_{\text{lens}}) = [0.01(M_{\odot}/M_{\text{lens}})^{1/2}, 0.1 M_{\odot}]$. We see that if the lens mass is small, the peak magnification is reduced but the variability timescale is near the same at this range, while the

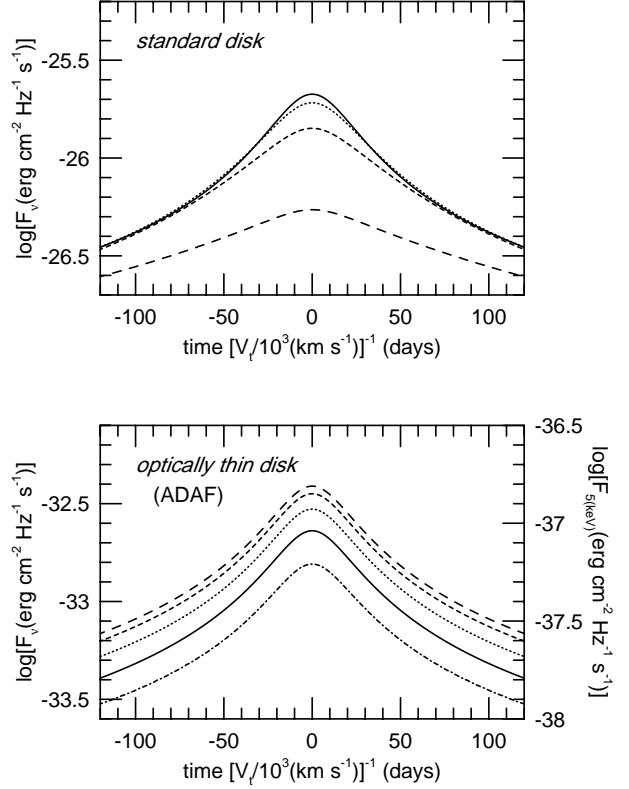


Fig. 7. Same as figure 6 but for the case with smaller lensing mass; $(b, M_{\text{lens}}) = [0.01(M_{\odot}/M_{\text{lens}})^{1/2}, 0.1 M_{\odot}]$ (Case 2).

chromaticity of the standard disk still remains. This is more clearly shown in table 1.

Next, in figure 8, we assign a larger impact parameter; $(b, M_{\text{lens}}) = (0.1, 1.0 M_{\odot})$ (Case 3). In this case, not only the total amplification become small but also chromaticity of standard disks no longer holds. Consequently, when we try to discriminate the disk structure, our success will depend not on the lens mass, but on whether the impact parameter is small or not. We will discuss this issue later (in section 4).

In table 1, we summarize characteristic values of these three light curves. Achromatic and chromatic features are clear in this table.

Finally, figure 9 shows the dependence of the spectrum on the lens mass. The smaller the lens mass is, the narrower the resulting shapes of the spectrum for a given flux value become. This is because when the lens mass is small, the Einstein-ring radius is small ($\theta_E \propto M_{\text{lens}}^{1/2}$, see Eq. [5]), so is the size of the region undergoing microlensing amplification. This reduces the total light amplification.

4. Discussion

We have demonstrated how spectral behavior and microlensing light curves depend on the disk structure. We

Case	disk model	band	$\log F_{(200d)}$	$\log F_{(100d)}$	$\log F_{(0d)}$	$\log[F_{(100d)}/F_{(200d)}]$	$\log[F_{(0d)}/F_{(100d)}]$
Case 1	standard	U	-26.179	-25.883	-25.174	0.296	0.709
		K	-26.288	-26.061	-25.766	0.227	0.305
	ADAF	U	-33.113	-32.820	-32.139	0.293	0.681
		K	-32.885	-32.592	-31.910	0.293	0.682
Case 2	standard	U	-26.667	-26.380	-25.674	0.287	0.706
		K	-26.775	-26.555	-26.264	0.220	0.291
	ADAF	U	-33.600	-33.317	-32.638	0.283	0.679
		K	-33.372	-33.089	-32.410	0.283	0.679
Case 3	standard	U	-26.340	-26.247	-26.203	0.093	0.044
		K	-26.446	-26.352	-26.311	0.094	0.041
	ADAF	U	-33.273	-33.180	-33.137	0.093	0.043
		K	-33.045	-32.952	-32.909	0.093	0.043

Table 1. The calculated fluxes at 3650Å (*U*-band) and 22000Å (*K*-band) at different epochs for case 1,2, and 3. Second, and third columns indicate the adopted accretion disk models and the energy band. Fourth, fifth, and sixth columns show the observed fluxes at $t = 200$ d (or -200 d), 100 d (or -100 d), and 0 d. Seventh and eighth columns display changes in the fluxes from $t = -200$ d to $t = -100$ d, and those from $t = -100$ d to $t = 0$ d, respectively. These two values are good indicators of the chromatic feature.

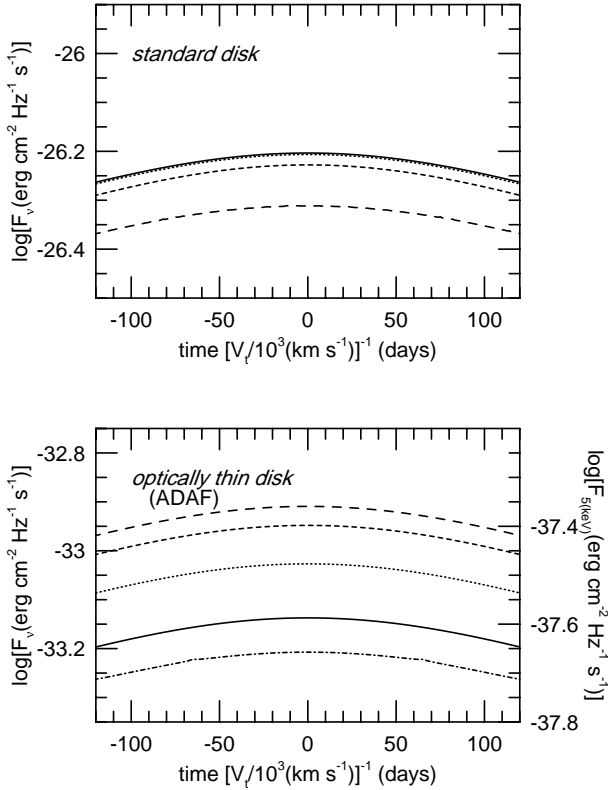


Fig. 8. Same as figure 6 but for the case with larger impact parameter; $(b, M_{\text{lens}}) = (0.1, 1.0M_{\odot})$ (Case 3).

considered two representative disk models: the standard-type disk emitting predominantly optical-UV photons, and the optically thin, advection-dominated flow (ADAF) producing a wide range of photons from radio to X- γ rays. Using the microlensing events, we can distinguish the different emissivity distribution of AGN accretion disks and

will be able to map them in details and reconstruct them from the light curves.

At the peak of the microlensing event, when the inner part of the accretion disk is largely amplified, distinctions between the two disk models are most evident (especially when the impact parameter is small). Thus, broad band photometry will be able to detect the color changes as shown in figure 6, thereby revealing the structure of AGN accretion disks.

Fortunately, such observations do not require good time resolution; for example, once per night like the MACHO project (e.g., Alcock et al. 1998) is sufficient, as long as a lens is located far from the observer. A typical timescale of microlensing event is characterized by the Einstein ring crossing time of a lens object expressed as

$$\frac{\theta_E}{v_t/D_{\text{ol}}} \simeq 6 \times 10^6 \left(\frac{M_{\text{lens}}}{M_{\odot}} \right)^{1/2} \times \left(\frac{v_t}{200 \text{ km s}^{-1}} \right)^{-1} \left(\frac{\tilde{D}}{10 \text{ kpc}} \right)^{1/2} \text{ s}, \quad (15)$$

where \tilde{D} means $D_{\text{ls}}D_{\text{ol}}/D_{\text{os}}$. For MACHO-like events when all the factors in the parentheses of eq. (15) are of the order of unity, the event timescales become ~ 0.2 yr. For the cosmological quasar case, on the other hand, we find roughly $\tilde{D} \sim 1 \text{ Gpc} = 10^5 \times 10 \text{ kpc}$, and thus, the third parenthesis became large by factor ~ 300 , yielding the event timescales being up to ~ 60 yr. Thus, in principle, a few years observation is sufficient to obtain the information about central disk structure. Practically, reconstruction from microlensing light curve that is so-called ‘inverse problem’ is not so easy, because, this requires a lot more to be done, e.g., take some (noisy, not perfectly sampled) light curve in a few filters. The source profile deconvolved by the observed light curve may comprise large

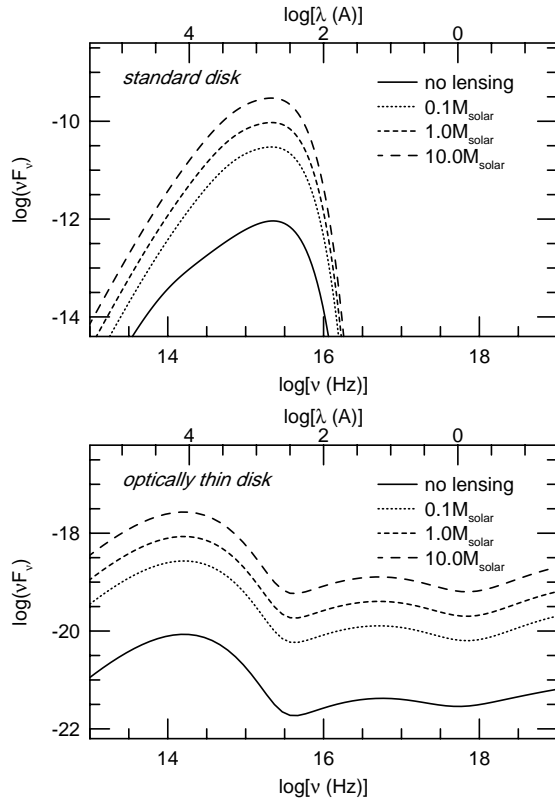


Fig. 9. Dependence of the microlensed spectra of the standard disk (upper) and the optically thin flow (lower) on the lensing mass, $M_{\text{lens}} = 0.1M_{\odot}$ (dotted line), $1.0M_{\odot}$ (dashed line), and $10.0M_{\odot}$ (long dashed line). The impact parameters are $0.01(M_{\odot}/M_{\text{lens}})^{1/2}$. The spectrum without microlensing is also plotted by the solid line.

errors, if the light curve sampling interval is much longer than the event duration timescale, or if the accuracy of the observed magnitude (i.e., flux from the source) is much poorer, as stated before by Grieger, Kayser, & Schramm (1991). Therefore, we need good time resolution not for discriminating accretion disk model, but for mapping detailed accretion disk. This reconstruction of accretion disk structure may be done in our future work.

To summarize the distinct properties of the two types of disks, we plot in figure 10 differences in the amplification factors at two different frequencies. Open and filled circles represent the cases with $b = 0.1$ and $b = 0.01$, respectively. The lensing mass is assumed to be $M_{\text{lens}} = 1.0M_{\odot}$. As the angular separation between the lens and the disk center (u) decreases, ΔF increases (thus the point moves in the upper right direction in figure 10). Obviously, the color changes are more pronounced in the right panel (between the U- and K-bands) than in the left panel (between the U- and V-bands), and for smaller impact parameters. We can easily discriminate the disk structure by comparing the optical and IR fluxes if $b \lesssim 0.03$. Furthermore, as

clearly seen in figure 10, the wider the separation between two observed wavelengths (or frequencies) are, the more apparent differences between the light curves of the two disk models become. Owing to this fact, the wider bands are preferable for more effective disk mapping.

As a first step to understand the microlensing phenomenon, we have considered microlensing by a single star in the present study. However, the microlensing events caused by a single lens, especially the case in which differences between the light curves of the two disk models are apparent (i.e., $b \leq 0.1$), seems not so frequent for the actual objects. We thus need to evaluate the average time interval $\langle \Delta t \rangle$ between microlensing events with an impact parameter smaller than b . From Paczyński (1986), we find that $\langle \Delta t \rangle$ is proportional to b^{-1} . If we regard the event that the impact parameter is $b \leq 1.0$ as the microlensing event, one microlensing event which we are interested in will occur among 10 ($b = 0.1$) to 100 ($b = 0.01$) events.

For example, we, here, assume the case of Q 2237+0305, although, in this case, single-lens assumption is not very good for this object because of its relatively large optical depth for microlensing (e.g., $\tau = 0.4 \sim 0.7$ from Rix, Schneider, & Bahcall 1992). It is widely believed that microlensing does occur in Q 2237+0305 at a rate of at least one event per year, i.e. $\langle \Delta t \rangle \sim 1\text{yr}$ (Corrigan et al. 1991; Houde & Racine 1994). Hence, the microlensing event which we would like to observe is expected to occur once per 10 yr (for $b = 0.1$) to 100 yr (for $b = 0.01$).

To conclude, microlensing events with such a small impact parameter may not be frequent, but once the microlensing with a small impact parameter occurs, a large light amplification is expected. We have demonstrated that an optically thick accretion disk exhibits more curious features in its spectral shape than an optically thin accretion disk. Differences between these two disk models are, essentially, caused by different energy balance equations. In an optically thick accretion disk, generally, viscosity is small, accreting gas stays in the accretion disk for a much longer time than the disk rotation periods, so that gravitational potential energy of accreting gas can be effectively transformed into radiation on its way to the central compact object (in the present case, a supermassive black hole). In an optically thin accretion disk, on the other hands, since viscosity is high, accreting gas falls into the central compact object rapidly in timescale on the order of the rotation period, and gravitational potential energy of accreting gas is not so effectively transformed into radiation (e.g., Kato, Fukue, & Mineshige 1998). Thus, most of gravitational potential energy of accreting gas is advected into the central compact object and is not radiated away. These major discriminant physical processes in the accretion disks can be distinguished by our microlens diagnostic technique.

In this paper, we assume that accretion disks are face on to the observer. In real situation, however, accretion

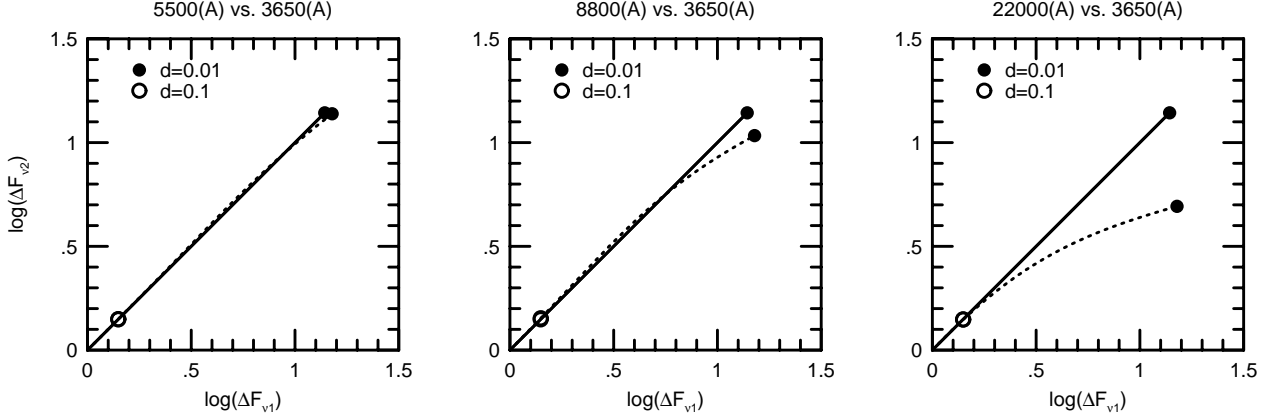


Fig. 10. Differences in the amplification factors at two different frequencies for the case of the standard disk (by the dotted line) and the optically thin flow (by the solid line), respectively. The adopted two frequencies are from the left, the U-band and the V-band (left panels), the U-band and the I-band (middle panels), and the U-band and the K-band (right panels), respectively. Open and filled circles represent the cases with $b = 0.1$ and $b = 0.01$, respectively. The lensing mass is assumed to be $M_{\text{lens}} = 1.0M_{\odot}$.

disks may have non-zero inclination angles (i.e., $i \neq 0$). It will be complicated to quantitatively treat the dependence of inclination angles because of the increase in the number of parameters, such as the angle between the path of the lens object and the apparent semi-major axis caused by a non-zero inclination. Qualitatively, non-zero inclination affects timescale of the microlensing event in such a way to reduce the apparent disk size by factor $\sim \cos i$. This effect seems to be small except the case that the disks are nearly edge on (i.e., $i \sim 90^\circ$). This inclination effect will be systematically examined in a future work.

Finally, recent high-resolution observations, including those from *HST*, have revealed circumnuclear starburst regions in AGNs (see Umemura, Fukue & Mineshige 1997, and references therein). If starburst regions exist around an accretion disk, microlensing event of AGN will make an interesting light curve; large-amplitude, short timescale variation (on a few months) caused by the microlensing of the accretion disk will be superposed on more gradual light variation (over a year) caused by the microlensing of starburst region (see figure 11). As shown in figure 11, the size of circumnuclear starburst regions is a tenth or hundredth as large as the central accretion disk. Hence, the microlensing timescale of circumnuclear starburst region is one tenth or hundredth as long as that of the accretion disk and the total amplification of the circumnuclear starburst region is smaller than that of the accretion disk from a rough estimate (see eq (2.28) of Schneider, Ehlers, & Falco (1992)). Thus, contributions of these two compositions to the microlensing light curve will be able to discriminate, and long-term monitoring may provide a possible tool to elucidate the extension of circumnuclear starbursts although the presence of intrinsic variability tends to make such analyses complex.

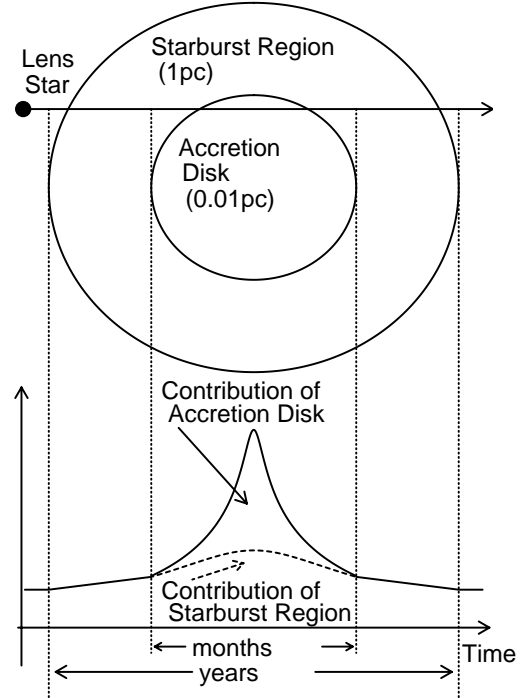


Fig. 11. Schematic view of a microlensing event of an AGN disk and circumnuclear starburst regions. Upper figure shows the situation of microlensing of accretion disk plus its circumnuclear starburst region. Lower figure shows its expected light curve.

5. Summary

The single-lens model as adopted in this paper is a good approximation, unless the apparent separations among

lens stars are appreciably smaller than the radius of the Einstein ring in the source plane. But, as we stated above, we should note that the images of Q2237+0305 could be subject to microlensing by multiple stars of the foreground galaxy. That is, we must consider, as a next step, the microlensing events caused by ‘caustics’ which is produced by multiple microlensing. Such events may occur more frequently with shorter durations and steeper magnification (Wambsganss & Kundić 1995). Light curves by the caustics will show even more interesting features than the present case (Schneider & Weiss 1986). More realistic, analytically approximated ‘caustic’ calculation has been done for the case of Q 2237+0305 (Yonehara et al. 1998).

This diagnostic method for the central region of AGN can be used in other sources (e.g., MG0414+0534, PG1115+080, and the so-called ‘clover leaf’, H1413+117 etc.). Future systematic and wide survey of quasars will discover other multiple quasars which our microlens diagnostic technique can apply.

Acknowledgements. We thank Joachim Wambsganß for valuable comments. We acknowledge the referee for his/her helpful indications and precious comments. One of the authors (A.Y.) also thanks Hideyuki Kamaya for his encouragement. This work was supported in part by Research Fellowships of the Japan Society for the Promotion of Science for Young Scientists, 9852 (A.Y.), by the Japan-US Cooperative Research Program which is founded by the Japan Society for the Promotion of Science and the US National Science Foundation, and by the Grants-in Aid of the Ministry of Education, Science, Sports and Culture of Japan, 08640329 & 10640228 (S.M.).

References

- Abramowicz, M.A., Chen, X., Kato, S., Lasota, J.-P., & Regev, O. 1995, *ApJ*, 438, L37
- Alcock, C., et al. 1998, *ApJ*, 499, L9
- Blandford, R.D., & Hogg, D.W. 1995, in *IAU Symp.* 173, *Astrophysical Applications of Gravitational Lensing*, ed. Kochanek, C.S., & Hewitt, J.N. (Dordrecht:Kluwer), 355
- Bontz, R.J. 1979, *ApJ*, 233, 402
- Bromley, B.C. 1996, *ApJ*, 467, 537
- Chang, K., & Refsdal, S. 1984, *A&A*, 132, 168
- Corrigan, R.T. et al. 1991, *AJ*, 102, 34
- Grieger, B., Kayser, R., & Refsdal, S. 1988, *A&A*, 194, 54
- Grieger, B., Kayser, R., & Schramm, T. 1991, *A&A*, 252, 508
- Houde, M., & Racine, R. 1994, *AJ*, 107, 466
- Huchra, J., Gorenstein, M., Horine, E., Kent, S., Perley, R., Shapiro, I. I., & Smith, G. 1985, *AJ*, 90, 691
- Irwin, M.J., Webster, R.L., Hewett P.C., Corrigan R.T., & Jędrzejewski, R.I. 1989, *AJ*, 98, 1989
- Jaroszynski, M., Wambsganss, J., & Paczyński, B. 1992, *ApJ*, 396, L65
- Kato, S., Fukue, J., & Mineshige, S. 1998, *BLACK-HOLE ACCRETION DISKS* (Kyoto, Kyoto University Press)
- Kundić, T. et al. 1997, *ApJ*, 482, 75
- Manmoto, T., Mineshige, S., & Kusunose, M. 1997, *ApJ*, 489, 791
- Narayan, R., & Bartelmann, M. 1996, *astro-ph/9606001*
- Narayan, R., & Yi, I. 1995, *ApJ*, 452, 710
- Paczynski, B. 1986, *ApJ*, 304, 1
- Padmanabhan, T. 1993, *Structure formation in the universe*, (New York, Cambridge University Press)
- Rauch, K.P., & Blandford, R.D. 1991, *ApJ*, 381, L39
- Rix, H.-W., Schneider, D.P., & Bahcall, J.N. 1992, *AJ*, 104, 959
- Rybicki, G.B., & Lightman, A.P. 1979, *Radiative Processes in Astrophysics*, (New York, Wiley)
- Schneider, P., & Ehlers, J., & Falco, E.E. 1992, *Gravitational Lenses*, (Berlin, Springer-Verlag)
- Schneider, P., & Weiss, A. 1986, *A&A*, 164, 237
- Shakura, N.I., & Sunyaev, R.A. 1973, *A&A*, 24, 337
- Umemura, M., Fukue, J., & Mineshige, S. 1997, *ApJ*, 479, L97
- Wambsganss, J., & Kundić, T. 1995, *ApJ*, 450, 19
- Wambsganss, J., & Paczyński, B. 1991, *AJ*, 102, 864
- Wambsganss, J., Paczyński, B., & Schneider, P. 1990, *ApJ*, 358, L33
- Yonehara, A., Mineshige, S., Manmoto, T., Fukue, J., Umemura, M., & Turner, E.L. 1998 *ApJ*, 501, L41
- Zheng, W., Kriss, G.A., Telfer, R.C., Grimes, J.P., & Davidsen, A.F. 1997, *ApJ*, 475, 469